AGU PUBLICATIONS

JGR

Journal of Geophysical Research: Atmospheres

RESEARCH ARTICLE
10.1002/2017JD027620

MJO-Related Intraseasonal Variation in the Stratosphere: Gravity Waves and Zonal Winds

M. J. Alexander[1], **A. W. Grimsdell**[1], **C. C. Stephan**[2], **and L. Hoffmann**[3]

[1]NorthWest Research Associates—Boulder Office, Boulder, CO, USA, [2]National Centre for Atmospheric Science-Climate, Department of Meteorology, University of Reading, Reading, UK, [3]Jülich Supercomputing Centre, Forschungzentrum Jülich, Jülich, Germany

Key Points:
- Numerical experiments investigate previously observed relations between intraseasonal stratospheric gravity wave and tropopause zonal wind variability
- Long vertical wavelength stratospheric wave variance is insensitive to MJO tropopause wind variations but highly sensitive to stratospheric winds
- Intraseasonal stratospheric zonal wind anomalies, likely driven by wave drag, are found to descend in altitude with increasing MJO phases 3 through 7

Supporting Information:
- Supporting Information S1

Correspondence to:
M. J. Alexander,
alexand@nwra.com

Citation:
Alexander, M. J., Grimsdell, A. W., Stephan, C. C., & Hoffmann, L. (2018). MJO-related intraseasonal variation in the stratosphere: Gravity waves and zonal winds. *Journal of Geophysical Research: Atmospheres*, *123*, 775–788. https://doi.org/10.1002/2017JD027620

Received 16 AUG 2017
Accepted 9 DEC 2017
Accepted article online 18 DEC 2017
Published online 19 JAN 2018

Abstract Previous work has shown eastward migrating regions of enhanced temperature variance due to long-vertical wavelength stratospheric gravity waves that are in sync with intraseasonal precipitation and tropopause wind anomalies associated with the Madden-Julian Oscillation (MJO). Here the origin of these intraseasonal gravity wave variations is investigated with a set of idealized gravity wave-resolving model experiments. The experiments specifically test whether tropopause winds act to control gravity wave propagation into the stratosphere by a critical level filtering mechanism or play a role in gravity wave generation through an obstacle source effect. All experiments use identical convective latent heating variability, but the large-scale horizontal wind profile is varied to investigate relationships between stratospheric gravity waves and zonal winds at different levels. Results show that the observed long vertical wavelength gravity waves are primarily sensitive to stratospheric zonal wind variations, while tropopause wind variations have only a very small effect. Thus, neither the critical level filter mechanism nor the obstacle source play much of a role in the observed intraseasonal gravity wave variations. Instead, the results suggest that the stratospheric waves follow the MJO precipitation sources, and tropopause wind anomalies follow the same sources. We further find evidence of intraseasonal wave drag effects on the stratospheric circulation in reanalyzed winds. The results suggest that waves drive intraseasonal stratospheric zonal wind anomalies that descend in altitude with increasing MJO phases 3 through 7. Eastward anomalies descend farther than westward, suggesting that MJO-related stratospheric waves cause larger eastward drag forces.

1. Introduction

Gravity waves are mesoscale phenomena that straddle the resolution limits of current global models used for long-range weather forecasting and climate prediction. Tropical gravity waves generated by convection are known to be important drivers of the general circulation and, in particular, the quasi-biennial oscillation (QBO) (e.g., Dunkerton, 1997; Holt et al., 2016; Scaife et al., 2000). The QBO, a reversal of the tropical lower stratosphere zonal mean winds on average every 28 months, is an important factor in long-range predictability of Northern Hemisphere winter weather (Scaife et al., 2014; Thompson et al., 2002). Gravity waves generated by tropical convection are also known to modulate the tropical tropopause cold point and the occurrence of cirrus clouds in the tropical tropopause layer (e.g., Jensen & Pfister, 2004; Kim & Alexander, 2015) and such thin cirrus produce more surface warming than thicker ice or water clouds (Stephens, 2005). Thus, studies of tropical gravity waves inform important processes in both weather and climate models.

On intraseasonal time scales, gravity wave variations have been previously observed in the tropical stratosphere and mesosphere with ties to convection within the Madden-Julian Oscillation (MJO) (Eckermann et al., 1997; Karoly et al., 1996; Moss et al., 2016; Rao et al., 2009; Tsuchiya et al., 2016). The MJO is a dominant mode of intraseasonal variability in tropical convection in the Eastern Hemisphere (Jiang et al., 2015; Madden & Julian, 1994; Waliser et al., 2009; Zhang, 2005). In particular, Tsuchiya et al. (2016) found a relationship between intraseasonal stratospheric gravity wave temperature variance observed by the Atmospheric Infrared Sounder (AIRS) and MJO precipitation and tropopause wind variations. They found that regional distributions of these quantities are synchronized with the MJO: The stratospheric gravity wave variances were larger for stronger precipitation anomalies and for stronger westward wind anomalies near the tropopause. In particular, the origin of the intriguing relationship between tropopause (100 hPa) westward winds (U_{100}) and stratospheric

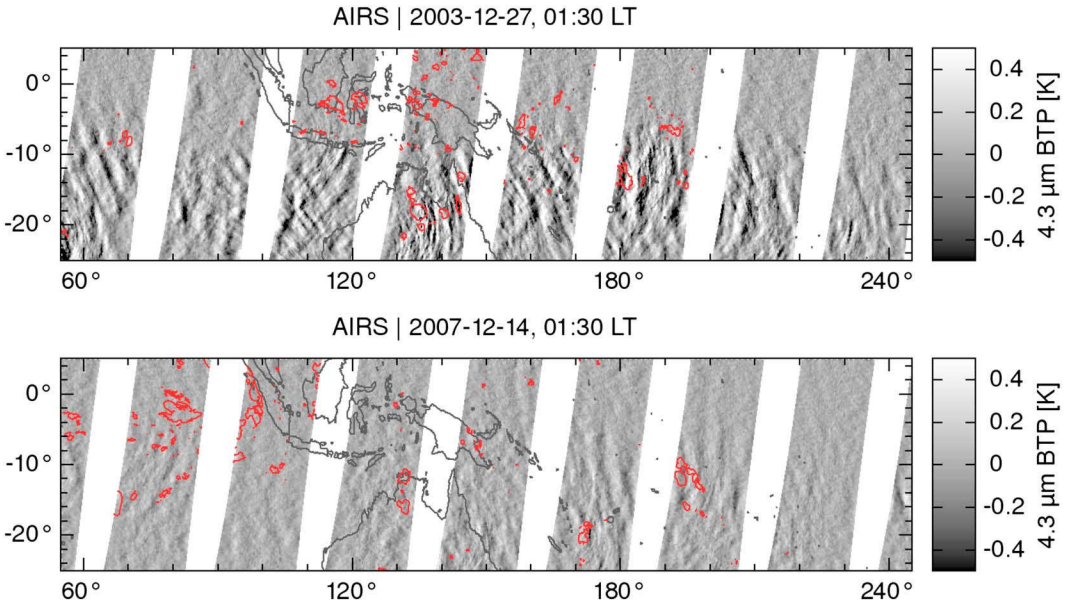

Figure 1. Two examples of daily AIRS nighttime brightness temperature coverage across the region of interest. Perturbations are saturated at ±0.5 K for better visualization of weak and strong waves. Red contours outline deep convective clouds, identified by AIRS 8.1 μm channel temperatures <210 K.

gravity wave temperature variance ($\hat{T}^2$) was proposed to have one of two causes: (1) reduction of eastward propagating gravity wave penetration into the middle atmosphere through critical level filtering and (2) a production of eastward propagating gravity waves through an obstacle effect source mechanism involving deep convection interacting with upper tropospheric winds. We note a third possible cause: (3) an AIRS observational filter effect associated with stratospheric winds and their relationship to U_{100}. The observed U_{100} relationship to $\hat{T}^2$ might also be due to any combination of these three factors.

In this work, we explore the mechanism behind this previously observed relationship between intraseasonal variability in AIRS stratospheric gravity waves $\hat{T}^2$ and winds near the tropopause U_{100}. We test the possible mechanisms through idealized modeling simulations in which some of the variable conditions are selectively held constant. We further explore possible wave drag effects of MJO-synchronized variations in gravity waves on stratospheric winds through examination of reanalyzed winds. We examine both MERRA-2 (Modern-Era Retrospective Analysis for Research and Applications version 2) (Bosilovich et al., 2015) and the original MERRA (Rienecker et al., 2011) reanalyzed winds. The tropical gravity wave parameterization was modified considerably for MERRA-2 in order to better simulate the QBO (Molod et al., 2015), so comparing these two reanalysis data sets provides an opportunity to examine MJO-related effects of parameterized gravity waves on global stratospheric winds. Following Tsuchiya et al. (2016), we focus on tropical latitudes between 20°S and the equator during the December through March periods beginning December 2003 ending March 2011.

Section 2 describes the precipitation data sets, reanalyzed winds, and AIRS observations of gravity waves that we use in this study. Section 3 describes the idealized modeling experiments. Section 4 shows results of these experiments and describes the role of tropopause and stratosphere wind variations on AIRS gravity wave temperature variance in the stratosphere. Section 5 examines relationships between MJO-related winds near the tropopause and in the stratosphere. Finally, section 6 is a summary with conclusions.

2. Data Description

2.1. AIRS Gravity Wave Observations

The AIRS instrument on the Aqua satellite measures radiances across a spectrum of infrared channels. The instrument scans across track, while the satellite motion along track provides a second dimension, creating image swaths that follow the orbit track. Hoffmann and Alexander (2010) averaged 42 AIRS channels in the CO_2 4.3 μm emission band in order to reduce the influence of noise in the data. We use these AIRS channel-averaged radiances converted to brightness temperature anomalies in this study. Figure 1 shows two typical examples of daily nighttime coverage across the study region. Wave anomalies are often visible as semicircular

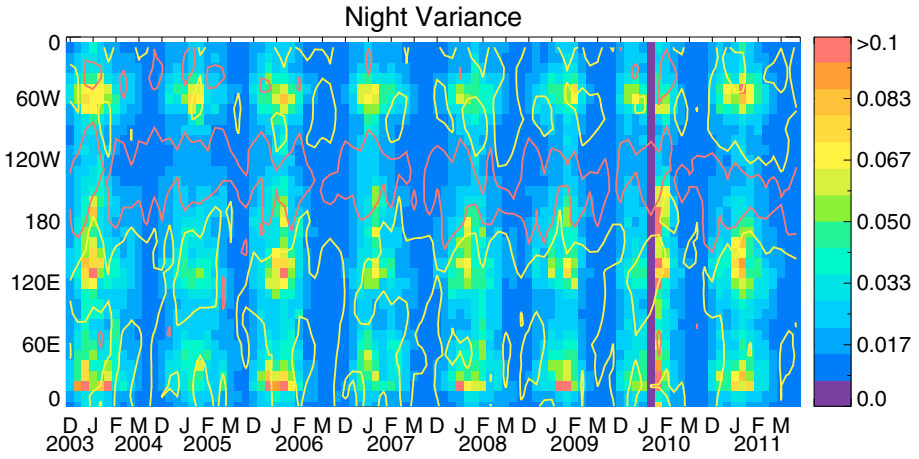

Figure 2. Tropical (0°–20°S) nighttime variance (K^2) for December through March from the 4.3 μm AIRS channels and the MERRA-2 zonal winds at 100 hPa (contour lines), including years 2003 to 2011. The red contour encloses zonal winds $>+5$ m s^{-1} and the yellow contour <-5 m s^{-1}.

arcs with center of curvature to the west, which are characteristics of eastward propagating stratospheric gravity waves at altitudes ~40 km that are emanating from precipitating convection in the troposphere below (Grimsdell et al., 2010; Stephan & Alexander, 2015). As can be seen in these two examples, the wave anomalies are generally weak directly on the equator and stronger toward 20°S.

The channel-averaged kernel function (which describes the vertical averaging of the temperature measurement) peaks near 30–40 km altitude. The vertical width of this kernel function is responsible for the fact that waves visible in AIRS stratospheric radiances and temperature retrievals generally have vertical wavelengths $\lambda_Z \geq 15$ km (Hoffmann & Alexander, 2009; Hoffmann et al., 2014). At λ_Z=15 km, the measured brightness temperature amplitude is 4% of the true temperature amplitude. Gravity wave theory tells us that λ_Z is roughly proportional to the intrinsic phase speed ($\hat{c} = c_0 - U$) of the wave. So there is an effect of the large-scale wind at the observation level U_{AIRS} on wave visibility, which is commonly called the observational filter (Alexander, 1998). For example, if $U(z)$ is the wind speed in the direction of wave propagation and considering the medium-frequency gravity wave dispersion relation for simplicity (Fritts & Alexander, 2003), then

$$|\lambda_Z(z)| = 2\pi|c_0 - U(z)|/N(z), \quad (1)$$

where N is the buoyancy frequency and c_0 is the ground-based phase speed of the wave. The altitude from which AIRS wave signals emanate depends on the combined effects of the kernel function, the wave vertical wavelength, the wave amplitude (which often grows with altitude), and measurement noise. This altitude will be close to ~40 km. As we will show later in section 5, the 40 km winds are generally westward ($U_{AIRS} < 0$) in the December–March season, so the waves visible to AIRS are generally propagating opposite to these winds (or eastward, $c_0 > 0$) in this season. Also, because the westward winds near 40 km altitude tend to increase in strength between the equator and 20°S (e.g., Ray et al., 1998), this observational filter effect also explains the larger wave amplitudes toward 20°S.

Tsuchiya et al. (2016) showed intraseasonal variations in AIRS nighttime gravity wave temperature variance averaged over 0–20°S during the December through March seasons (2003 to 2011). The temperatures they used were specialized high horizontal resolution temperature retrievals derived from AIRS for stratospheric altitudes (Hoffmann & Alexander, 2009) that were averaged in height. Tsuchiya et al. (2016) chose nighttime data from altitudes near the 4.3 μm kernel function peak where noise is minimized. Because we are using AIRS brightness temperatures rather than retrievals, we repeat the analysis of Tsuchiya et al. (their Figure 1c) here in our Figure 2 using radiances instead of retrieved temperatures. We utilize here the same 10 day, 0–20°S latitude, and 10° longitude averaging bins and choose nighttime only data. Figure 2 also overlays the same ±5 m s^{-1} U_{100} wind contours. The temporal and longitudinal variations in gravity wave variance are almost identical to Tsuchiya et al. (2016), and we see the same relationship where variance tends to peak where U_{100} is westward. (Note that the black bar is a period with no measurements, and the following 10 day period had only 30% of normal coverage.)

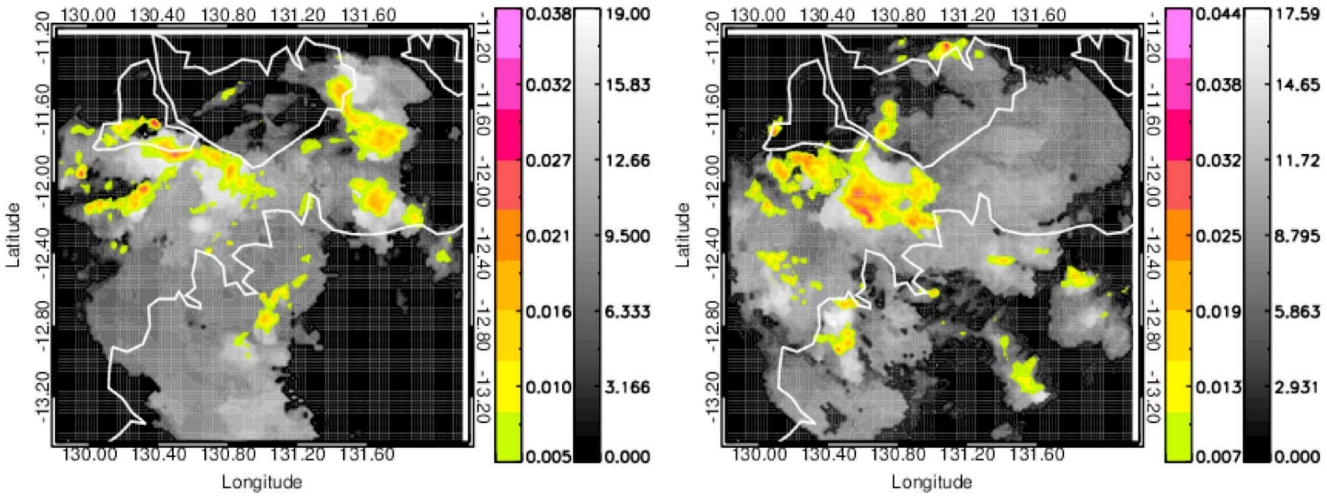

Figure 3. Snapshots showing properties of precipitation and latent heating derived from the Gunn Point scanning radar north of Darwin, Australia. Panels show radar-observed echo top height (gray scale, km), and column-integrated latent heating (color, K s^{-1}) at 15:00 UT (left) and 17:00 UT (right). White contours show coastal outlines. These are based on observations obtained on 23 January 2006 (active monsoon period) (May et al., 2007).

2.2. MERRA Reanalyses

The Modern-Era Reanalysis for Research and Applications version 2 (MERRA-2) (Bosilovich et al., 2015) is utilized here to define 10 day average wind and static stability conditions that influence wave propagation and generation. Equatorial reanalyzed stratospheric winds within ±10° are not well constrained by observations (Baker et al., 2014) because wind measurements are scarce and there does not exist a predominant balance between the mass and wind field close to the equator (Žagar et al., 2013). Thus, the more abundant temperature soundings provided by satellite do not constrain the wind close to the equator, and equatorial winds in analyses are primarily constrained only by radiosondes in the stratosphere (below 30 km) launched at a limited number of tropical stations. These are supplemented by cloud-tracked winds in the troposphere. Podglajen et al. (2014) compared tropical analyzed winds at ~20 km to measurements during the Pre-Concordiasi long-duration balloon campaign and revealed large errors, particularly in the Indian and Pacific Oceans where radiosonde measurements are lacking. At higher latitudes, balanced winds derived from satellite temperature sounding measurements become better constrained at least up to ~40 km. In the upper stratosphere and mesosphere, constraints are weak globally. Keeping these uncertainties in mind, section 5 will compare winds averaged 0° – 20°S to those averaged 10° – 20°S where uncertainties are smaller.

Above 40 km, the influence of parameterized gravity wave drag in the underlying model in the reanalysis system becomes increasingly important. Fortunately, for our purposes, the tropical gravity wave parameterization was changed significantly when the next generation MERRA-2 reanalysis was developed (Gelaro et al., 2017). Molod et al. (2015) show that parameterized tropical gravity wave stress was increased by a factor of 10 equatorward of 15° in order to improve simulation of the QBO. This changed the gravity wave drag from MERRA to MERRA-2, which provides a natural experiment we can use to examine the effects of parameterized gravity wave drag on the reanalyzed tropical winds. We therefore also compare results with MERRA-2 and MERRA reanalyses in section 5.

2.3. Precipitation Measurements

We employ a variety of precipitation measurements in this study.

Scanning radar measurements. Local scanning radar measurements are used for idealized gravity wave-resolving model studies. We use rain rate and echo-top-height retrievals from the Gunn Point C-POL radar at 131.04°E and 12.25°S in Northern Australia (Keenan et al., 1998) on 23 January 2006. This is a period when the MJO was active in the region (May et al., 2007). The observations will define a spatially and temporally varying latent heating field that forces gravity waves in idealized model runs. The method for converting radar rain rate and echo top height to three-dimensional time-varying latent heating was described in Grimsdell et al. (2010). The latent heating field will be identical in all the idealized model experiments to focus on how wind variations affect the stratospheric gravity waves. This latent heating source is thus a controlled variable in the experiments. Two instantaneous maps of the column integrated latent heating and echo top heights at 15:00 and 17:00 UT are shown in Figure 3.

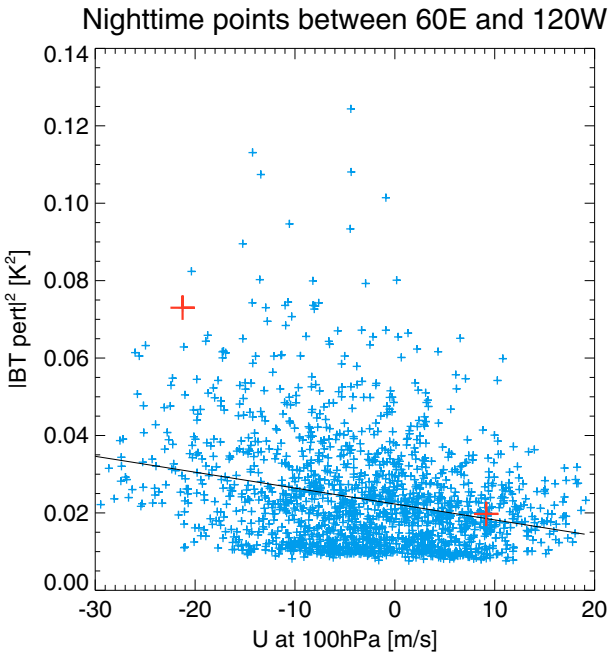

Figure 4. Nighttime variance in 4.3 μm channels versus U_{100} (m s^{-1}). Each symbol represents one 10 day and 10° longitude averaged point in Figure 2. The red symbols are those selected to represent different wind and gravity wave variance conditions. (See text.) Black line is a linear least squares fit to the data.

Tropical Rainfall Measuring Mission (TRMM) rain rates. Instantaneous rain rates are available as Tropical Rainfall Measuring Mission (TRMM) satellite products throughout our study period. The 3B42 product is available at 0.25°×0.25° and 3-hourly resolution at all tropical latitudes (Huffman et al., 2007). In designing the model experiments presented in section 3, regional mean precipitation and precipitation variance are evaluated. We use the TRMM 3B42 product for this purpose.

Global Precipitation Climatology Project (GPCP) rain rates. Global daily mean rain rates are available at 1°×1° resolution through the Global Precipitation Climatology Project (GPCP) (Huffman et al., 2001; Xie et al., 2011). The daily GPCP data are a well-calibrated data source for defining long-term precipitation variability. Tsuchiya et al. (2016) used these data to define relationships between intraseasonal precipitation variability, 100 hPa winds, and stratospheric gravity wave activity. We use these data to define longitudinal variations in the climatology of intraseasonal precipitation in section 5.

2.4. MJO Index

The real-time multivariate MJO (RMM) index (Wheeler & Hendon, 2004) is used to identify MJO strength and phase as a function of time. The data source is the National Centers for Environmental Prediction operational data (Wheeler & Hendon, 2016). The index is based on patterns observed in outgoing longwave radiation and zonal wind at 850 hPa and 200 hPa. The RMM index magnitude and phase time series for the period of interest were shown in Tsuchiya et al. (2016). Following that earlier work, RMM > 1 is used to indicate significant MJO activity and identify days included in MJO composite averages.

3. Experiment Design

Figure 4 shows a scatterplot of intraseasonal gravity wave variances and zonal winds at 100 hPa (U_{100}). Each symbol represents a point on the time versus longitude plot in Figure 2. As explained earlier, these are averages between 0° and 20°S latitude during the December through March season. While linear correlation is not strictly valid due to the non-Gaussian distribution of the points, it is clear that the highest variances occur more frequently in conditions with westward U_{100}, the same relationship identified by Tsuchiya et al. (2016).

The two red pluses highlight two points that show strong differences in both U_{100} and gravity waves. Table 1 describes the regional winds, waves, and precipitation observed during these two 10 day periods. The mean U_{100} is strong westward in one case (−20.8 m s^{-1}) and eastward in the other case (+9.1 m s^{-1}). Gravity wave brightness temperature variances differ by 365%. Despite these large differences in U_{100} and gravity waves, both cases include significant precipitation and precipitation variability (Table 1), an indication of convective gravity wave sources. In the strong gravity wave case, mean precipitation rates were 32% larger, and precipitation variance was larger by 26%. Although these are not negligible differences, they are relatively minor compared to the 365% difference in the gravity wave brightness temperature variance. We devise a set of idealized gravity wave model experiments that eliminate these relatively small precipitation differences entirely in order to examine the role of horizontal wind profile changes in isolation from other variables. In particular, we focus on U_{100} (at ~16 km) and zonal winds at 40 km (U_{AIRS}) in order to better understand what causes the large gravity wave changes observed by AIRS.

Table 1
Rain and Wind Conditions for Two Regions/Periods Identified With Red Pluses in Figure 4

Date range	Longitudes	U_{100}	GW variance	Mean rain[a]	Rain variance[a]
21–30 Dec 2003	130–140°E	−20.8 m s^{-1}	7.3 ×10^{-2} K^2	0.46 mm h^{-1}	2.2 (mm h^{-1})^2
11–20 Dec 2007	170–180°E	+9.14 m s^{-1}	2.0 ×10^{-2} K^2	0.33 mm h^{-1}	1.7 (mm h^{-1})^2

[a]As defined by the TRMM 3B42 data product.

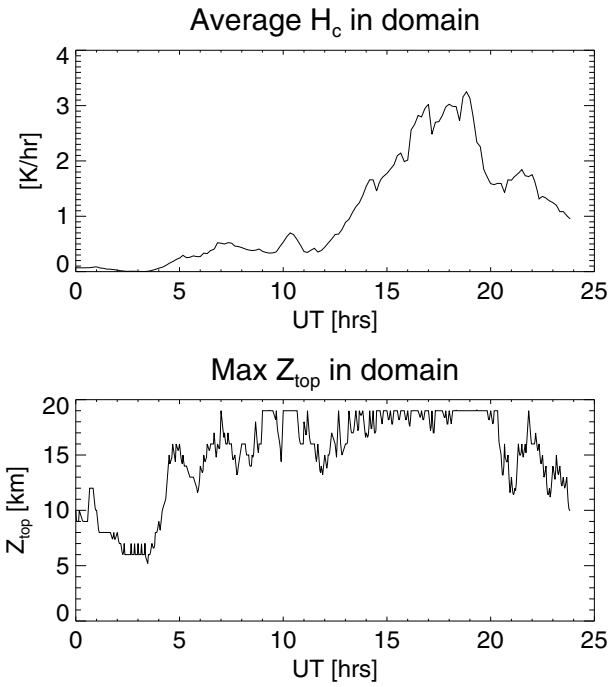

Figure 5. Domain-averaged column heating (H_c, K h^{-1}) and domain maximum echo top height (Z_{top}, km) as functions of time at 10 min resolution. The model is initialized at 15:00 UT in each experiment.

3.1. Idealized WRF Model

To isolate the effects of different wind profiles on gravity wave variance, we utilize idealized Weather Research and Forecasting (WRF) model simulations that are forced with prescribed latent heating $Q(x, y, z, t)$ in the troposphere, which acts as a controlled source of gravity waves. This idealized WRF model (Stephan & Alexander, 2015) provides a way to control the gravity wave sources in order to isolate the effect of the horizontal wind on gravity waves. Briefly, it is a dry idealized version of WRF with cumulus, microphysics, radiation, surface, and boundary layer schemes turned off. The model is initialized with uniform profiles of horizontal wind and potential temperature and no topography.

Our simulations are forced with latent heating $Q(x, y, z, t)$ that is based on the varying precipitation rates R and echo top heights Z_{top} from Gunn Point radar observations in North Australia (see Figure 3). At each point in space and time, heating profiles have an assumed half-sine profile shape following Grimsdell et al. (2010):

$$Q(z) = \frac{\pi}{2} H_c \sin\left(\frac{\pi z}{Z_{top}}\right), \tag{2}$$

and $Q = 0$ at the surface ($z = 0$) and $z > Z_{top}$. The column heating H_c is

$$H_c = 3.8 \frac{R \rho L_c}{C_p M}. \tag{3}$$

Here ρ is the density of water, L_c is the latent heat of condensation, C_p is the heat capacity of air, and M is the column-integrated density of the air below Z_{top} weighted by the half-sine profile shape. The factor 3.8 is empirical as derived in Grimsdell et al. (2010), but it loosely represents the effects of horizontal transport of condensate, evaporative cooling, and ice formation (Stephan & Alexander, 2015) that are missing in this simple relationship. We do not use the profile in Stephan and Alexander (2015) because that profile was developed for summertime midlatitude convection over the Continental United States, whereas our case is tropical.

The model's horizontal domain is on a 600 km × 600 km Cartesian grid with 2 km resolution. $Q(x, y, z, t)$ is defined on the 2 km, 10 min resolution of the radar data but is interpolated in time to the 2 min time step utilized in the model. The heating is only nonzero within a 250 km radius area, which is centered within the model domain. Vertical resolution is a constant 500 m between the surface and the model top at 55 km. The top 5 km layer of the domain is a sponge. (See Stephan & Stephan, 2015, for additional details.)

All experiments will utilize the same $Q(x, y, z, t)$ to force waves in the idealized model. Only the wind profiles vary among experiments. R and Z_{top} variations on 23 January 2006 are illustrated in Figure 5 by showing the time series of the areal-averaged column heating rate and the domain maximum echo top height. All simulations are initialized with domain average profiles of horizontal wind and potential temperature, and heating rate conditions start with those at 15:00 UT and run for 6 h. Results are shown between 17:00 and 21:00 UT, and we also show 17:00–20:00 UT time means of wave variance when the convection is strongest (Figure 5).

4. Model Experiments and Results

Five experiments are performed to better understand the effects of the horizontal winds on modeled gravity wave variance. Each case is coded with a different color in Figures 6–8. The convective gravity wave forcing in the troposphere is artificially specified to be the same in all experiments in order to isolate the effects of the background wind.

Cases 1 and 2 have background conditions of the two selected 10 day regional average points in Figure 4 (see Table 1). In Figure 6, Case 1 (red) uses the horizontal wind profiles of the strong gravity wave case. Case 2 (gold) is the weak gravity wave case. Note the different scales for the zonal (U) and meridional (V) winds. The U differences in the upper troposphere are large, nearly 30 m s^{-1} at 16 km (100 hPa), and also large differences occur in the upper stratosphere. The V and temperature differences are relatively minor, with differences in

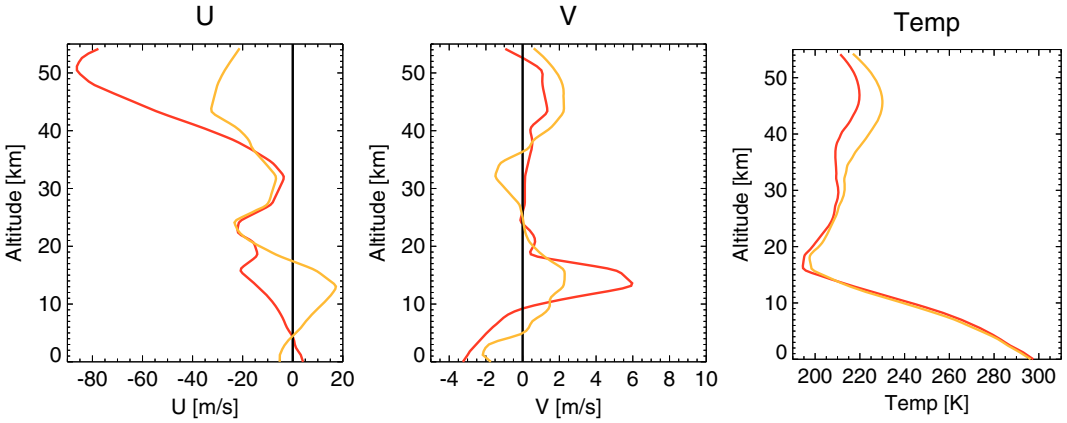

Figure 6. MERRA *U*, *V*, and *T* profiles for the two selected cases: Case 1 (red) and Case 2 (golden). These profiles were used as input to the model experiments.

static stability N<5% and proportionate small effects on λ_Z through (1). Possible effects of these V or N differences on gravity wave visibility are anticipated to be <20%, whereas we are looking to explain a factor of ~3 in gravity wave variance. We therefore concentrate on the effects of the differences in U.

Cases 3 and 4 (Figure 7) differ only in the tropospheric wind. Case 3 (green) matches Case 1 winds up to 22 km, but in the stratosphere above 22 km winds are modified to be the average of Cases 1 and 2. Case 4 (blue dashed) matches Case 2 winds up to 22 km, but like Case 3, it is an average of Cases 1 and 2 in the stratosphere. We chose 22 km to distinguish troposphere from stratosphere winds because this altitude is well above any wave source effects that can occur as high as the tropopause while still well below the AIRS observation altitudes. Case 1 and Case 2 winds are very similar at 22 km, so this choice also avoids any artificially large shears in the modified wind profiles.

Stratospheric gravity wave variances for these four cases are summarized in Figure 8. Variances here are computed from modeled temperatures converted to brightness temperature using the AIRS kernel. Variance about the mean brightness temperature is computed at 3 min intervals. Note that these variances are much larger than those in Figure 4 because we average here only during a short active period and over a smaller area, while Figure 4 included both quiet and active times during a 10 day period and 10° × 20° area. The curves in Figure 8 show pulses in variance associated with changes in the wave forcing (Q), and these pulses then arrive at slightly different times in the stratosphere depending on the wave packet group velocities, which depend on the winds. Case 1 (red) has by far the largest gravity wave variance. The color-coded numbers show the

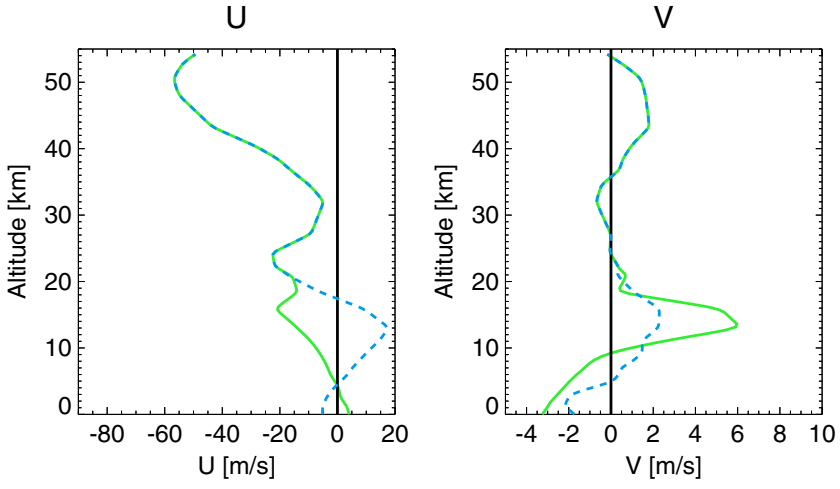

Figure 7. Input *U* and *V* profiles for the stratosphere-modified cases: Case 3 (green) and Case 4 (blue dashed). These profiles were modified so that *U* and *V* are identical above 22 km.

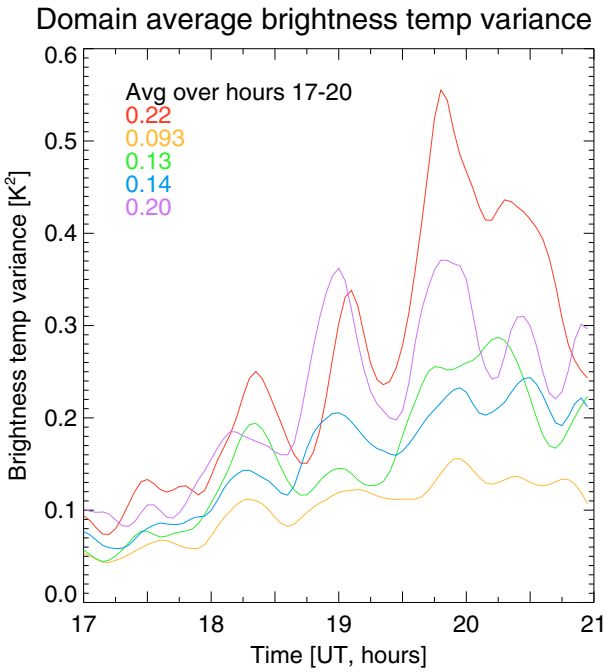

Figure 8. Modeled domain-averaged gravity wave variance (K^2) as a function of time for each of the five experiments: Case 1 (red), Case 2 (gold), Case 3 (green), Case 4 (blue), and Case 5 (purple). Variances averaged over hours 17:00–20:00 UT are printed in the legend.

average of hours 17:00–20:00 UT when the gravity wave forcing in the model is strongest. Case 1 variance is 240% larger than Case 2 (gold) averaged over these 3 h, and the peak value is 350% larger, comparable to the 365% difference in Table 1. These differences between Case 1 and Case 2 demonstrate that sources for these two regions/periods are not a major factor in explaining the differences in variance because the sources $Q(x, y, z, t)$ were the same in both experiments, and zonal wind differences must be responsible.

Figure 8 gravity wave variances for Cases 3 are 4 are relatively very similar to one another, and they fall in between the two extremes of Cases 1 and 2. Cases 3 and 4 differ only in tropospheric wind, and the effect is only ~10% in the 3 h mean. Variances among Cases 1–4 roughly scale with the strength of the stratospheric wind. From this result, it appears that the tropopause wind has only a secondary effect on the gravity wave variance in the stratosphere.

To further test this effect of troposphere versus stratosphere wind, we completed a fifth experiment Case 5, which uses Case 2 winds (gold) in the troposphere up to 22 km and Case 1 winds (red) in the stratosphere above 22 km. Case 5 gravity wave variance is plotted as the purple curve in Figure 8. It does not quite achieve the highest wave activity of Case 1, but Case 5 and Case 1 are quite similar in the 3 h mean variance, again differing by only ~10%. This confirms that the stratospheric winds have the largest effect on the gravity wave brightness temperature variances, while U_{100} tropopause winds have a secondary, much smaller effect.

To understand these results, we must consider the vertical kernel function associated with the AIRS measurements. For both brightness temperatures and retrieved temperatures, gravity waves with vertical wavelengths less than 15 km are severely attenuated in AIRS data.

Figure 9 shows theoretical vertical wavelengths versus altitude above the tropopause for four waves with different ground based zonal phase speeds $c_0 = 0$, 10, 20, and 30 m s^{-1} using the theoretical dispersion relation (1). Gray shading masks vertical wavelengths that are not generally visible in the AIRS measurements ($\lambda_Z \leq 15$ km). The dotted line marks the altitude where the AIRS measurements are most sensitive (~40 km). $c_0 = 0 - 10$ m s^{-1} covers the range of MJO propagation speeds, so we might expect waves generated by eastward moving deep convection interacting with shear near the tropopause (the so-called "obstacle effect," Pfister et al., 1993) to have phase speeds in this range (Alexander et al., 2006). Spectra of waves generated by a deep convective heating mechanism often peak at somewhat faster speeds, near $c_0 = 20$ m s^{-1} (Beres et al., 2004), and even faster waves are also generated although with weaker amplitudes.

The two panels show $\lambda_Z(z)$ for Case 1 (left) and Case 2 (right) zonal winds. Waves with $c_0 = 0$ m s^{-1} have short λ_Z throughout the stratosphere. For Case 2, these waves have a critical level near 18 km, which prevents them from propagating further into the stratosphere. Slow waves are the waves most likely to be affected by wind filtering, but they are not visible in AIRS data ($\lambda_Z < 15$ km). Waves with $c_0 = 10$ m s^{-1} are similarly too short to be visible to AIRS. Other detection methods such as radiosonde or radio occultation profiling (Karoly et al., 1996; Moss et al., 2016) would detect these shorter λ_Z waves, and hence, tropopause wind filtering may more likely modulate gravity wave variance, but not in AIRS data. Higher phase speeds $c_0 = 20$ m s^{-1} become visible to AIRS, and the differences between the two cases help to explain why the simulated AIRS variance is stronger in Case 1 than Case 2. This wind effect may also explain why the perturbations shown in Figure 1 and Table 1 were so much stronger in late December 2003 than in mid-December 2007. Faster waves ($c_0 \geq 30$ m s^{-1}) would be visible in both cases.

The variances in Figure 8 were brightness temperature variances, simulated by application of the AIRS vertical kernel function. Throughout the December through March period of interest, the stratospheric winds are, in fact, westward, and these westward winds give eastward propagating waves much longer vertical wavelengths than westward propagating waves. Thus, only eastward waves survive the observational filter.

The so-called obstacle effect mechanism for gravity wave generation (Pfister et al., 1993) does not appear to be important for the gravity waves observed by AIRS in our cases. If it were important, the strong upper

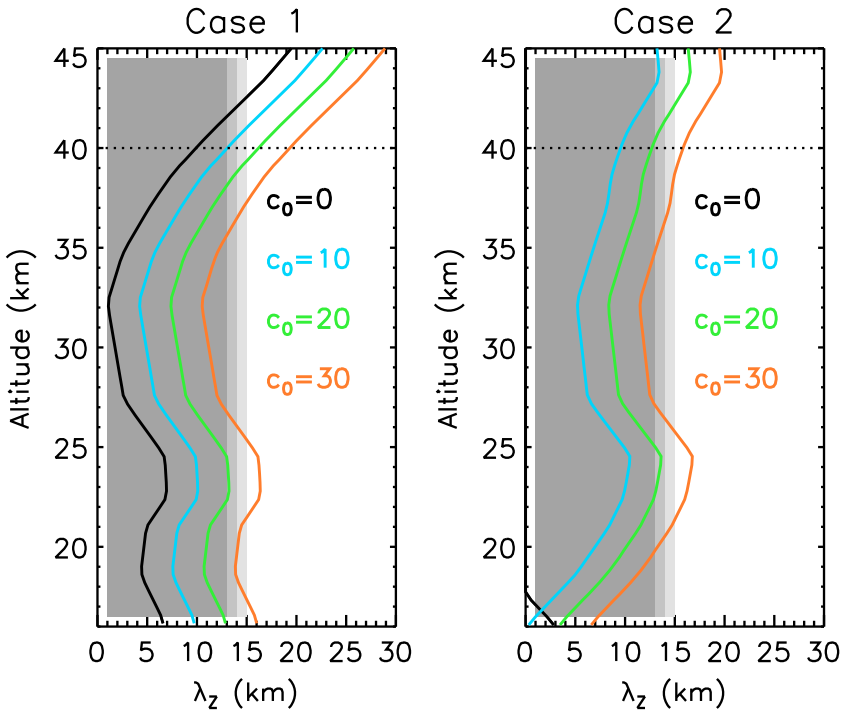

Figure 9. Theoretical vertical wavelengths (λ_Z) for gravity waves color coded by their ground based phase speed (c_0 in m s^{-1}) assuming Case 1 (left) and Case 2 (right) zonal winds. The gray shaded region masks vertical wavelengths that are rarely visible in AIRS observations, and the horizontal dashed line marks 40 km where the 4.3 μm AIRS measurements are most sensitive.

tropospheric westward wind of Case 1 would include an important source of eastward propagating waves that would be absent in Case 5. While this source mechanism may still be active for waves generated by MJO-related convection (Evan et al., 2012), these waves do not apparently contribute much to AIRS variance, probably because they would have slow c_0 and they would not have sufficiently long vertical wavelengths in the stratosphere to survive the AIRS observational filter. We note that other observation techniques such as radio occultation (Moss et al., 2016) or radiosonde (Karoly et al., 1996) profiling would in contrast be much more likely to detect waves with slower c_0. So our conclusions about the source mechanism are not general but specific to gravity waves with faster c_0 (>20 m s^{-1}), such as those observed by AIRS.

In summary, the stratospheric wind speed has dominant control over the AIRS gravity wave variance, with changes up to 350% seen in the cases studied here (240% in the 3 h mean). Conversely, tropopause winds have only a minor secondary effect, with an effect of only ~10% in the gravity wave variance. Important questions remain: Why does the tropopause wind show a strong correlation with AIRS variance in the observations? Are the tropopause winds and stratospheric winds correlated as well? We investigate these question in the next section.

5. MJO-Related Wind Variability

Meridionally averaged (0°–20°S) zonal winds from MERRA as a function of longitude and altitude are shown in Figure 10a. Each panel in the column represents the composite average wind for all days when the RMM index exceeded a value of 1 for a given phase of the MJO. As before, only data from December to March periods within December 2003 through March 2011 are included in order to match the analysis in Tsuchiya et al. (2016). Eight panels progress from phase 1 (top) to phase 8 (bottom).

Figure 10a shows that stratospheric winds in these phase composites are uniformly westward with rather small longitudinal variations. The December–March period is a time when the stratospheric semiannual oscillation (SAO) is westward (Garcia et al., 1997; Ray et al., 1998), and the SAO is clearly dominating the stratospheric wind in these composites. Since the focus here is on the intraseasonal variability, we compute a matching set of longitude-height wind composites (Figure 10b) made from climatological monthly means

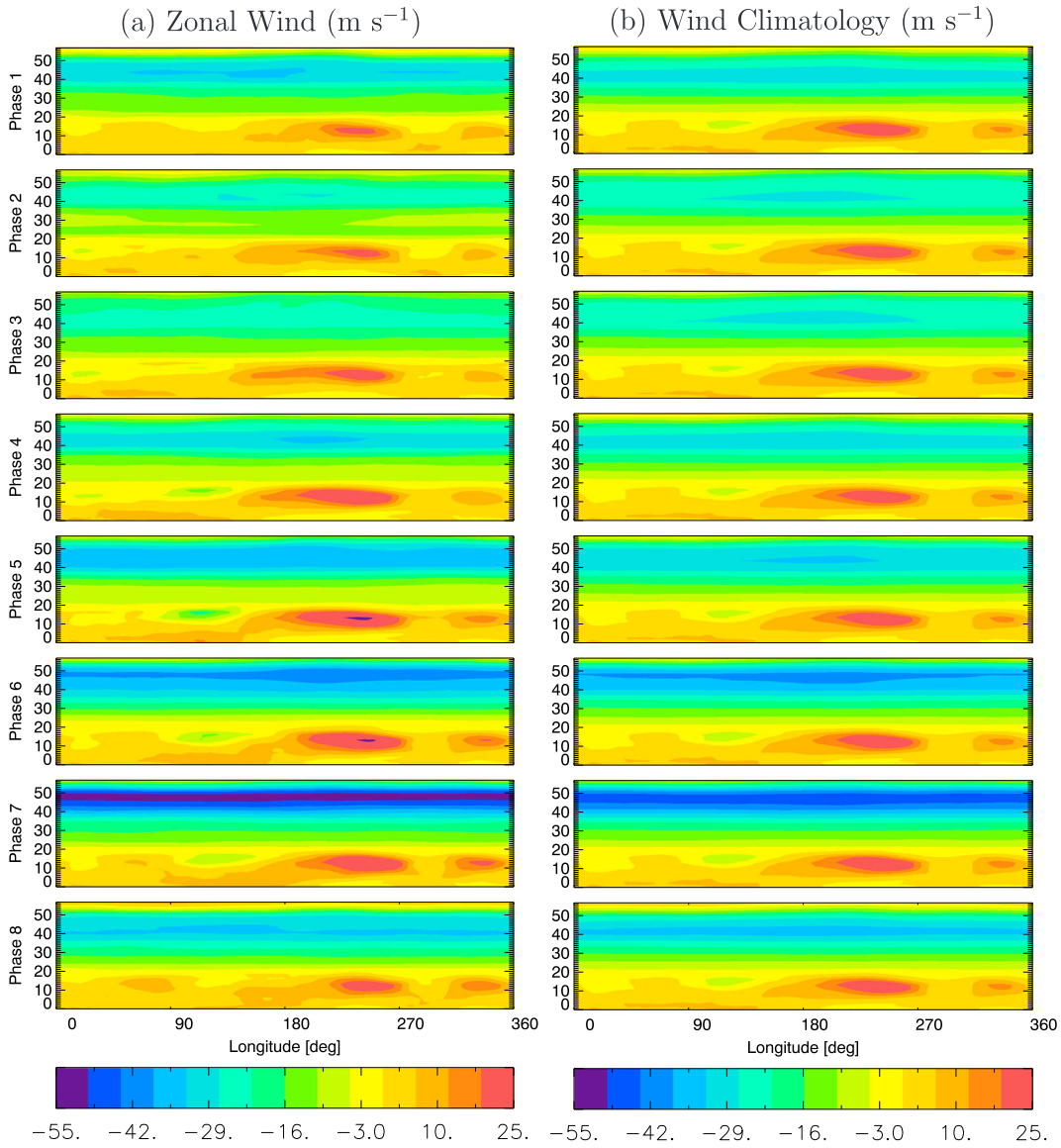

Figure 10. Two columns each showing 0–20°S zonal winds (m s^{-1}) as a function of longitude and height (km) for the eight MJO phases (top to bottom). (a) MERRA-2 zonal wind composites for each MJO phase considering only days where the RMM index is >1. (b) MERRA-2 wind 2003–2011 climatology, where each panel (top to bottom) shows monthly mean zonal wind weighted by the frequency of occurrence of that month in each MJO phase but otherwise not considering the RMM index. Figures 10a and 10b look similar, due to the climatological phase of the stratospheric seminannual oscillation (SAO) in the December through March period.

and weighted by the monthly occurrences of each MJO phase but otherwise without reference to the RMM index. For example, for the phase 1 MJO composite in Figure 10a: 12% of the points were from December, 29% from January, 18% from February, and 41% from March. Figure 10b uses these fractions and the climatological monthly mean winds. Figures 10a and 10b look very similar, but the differences, shown in Figure 11, reveal wind anomalies specifically associated with the MJO. The climatological SAO seasonal variation has been removed. Intraseasonal GPCP precipitation is composited the same way, and the differences between days with RMM>1 and the climatology, averaged between 20°S and 10°N, are marked with the black bars in Figure 11 wherever they exceed 1 mm h^{-1}.

In Figure 11 we can trace the eastward motion of MJO precipitation through phases 2–7. In the troposphere, we can also see lower troposphere westerly wind anomalies topped by upper troposphere easterly anomalies that roughly follow the eastward motion of the intraseasonal precipitation anomalies. There is some indication

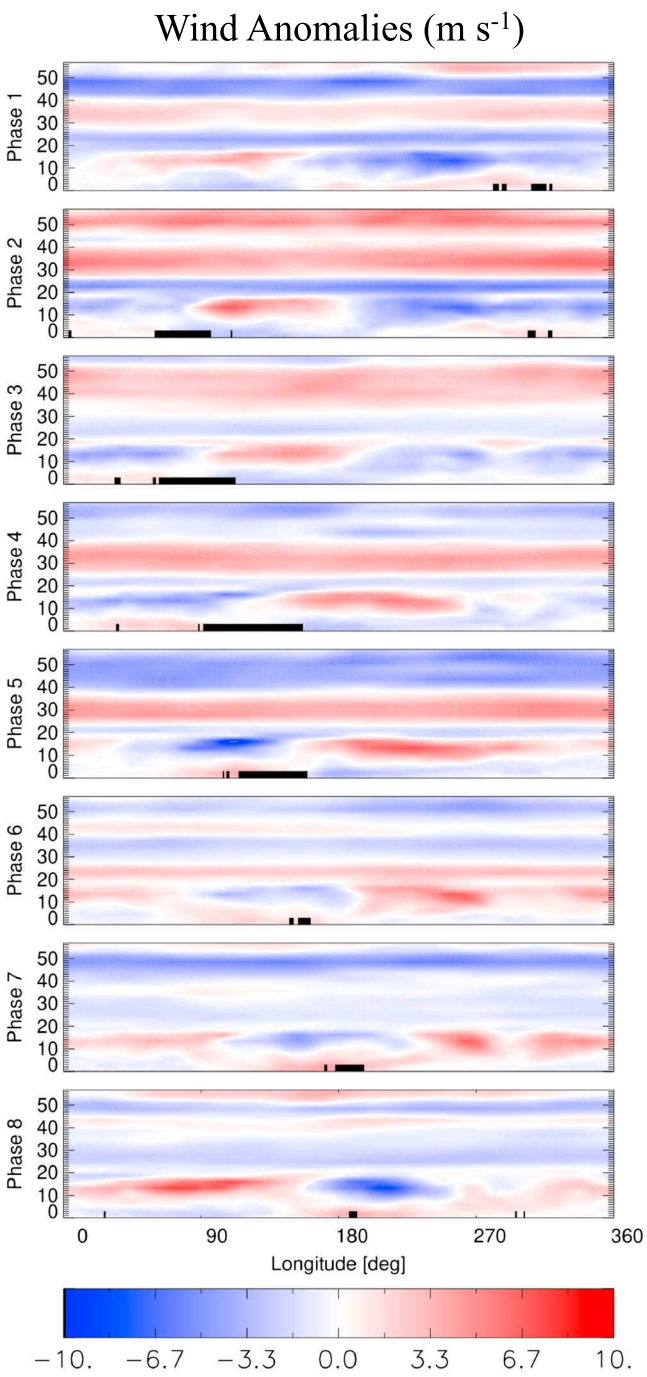

Figure 11. MERRA-2 intraseasonal 0–20°S zonal wind anomalies (m s^{-1}) as a function of longitude and height (km) for the eight MJO phases (top to bottom). These are the differences between Figures 10a and 10b, which isolates the MJO signal. Bars at the bottom of each panel show where intraseasonal rain rate anomalies exceed 1 mm h^{-1}.

from these panels that the MJO precipitation occurs more often in regions where upper troposphere winds are easterly, but this is clearer in the latitudinally resolved maps shown in Tsuchiya et al. (2016) (see supporting information Figure S1). Our results suggest that this relationship between MJO precipitation and upper tropospheric easterly wind anomalies is the likely reason for the correlation of stratospheric gravity waves and U_{100} that was found in Tsuchiya et al. (2016).

What Figure 11 also shows is the MJO-related wind anomalies in the stratosphere. In particular, there is evidence of descent of wind anomalies with MJO phase, analogous to the descent of the QBO wind anomalies, but here on intraseasonal time scales. Because these anomalies do not show much longitudinal variation, we zonally average Figure 11 and the result is Figure 12a. Here we can more clearly see the descent of the wind anomalies with MJO phase. Eastward wind anomalies are plotted with solid lines and show clear descent through the stratosphere from phases 3 to 6. Westward wind anomalies are plotted with dashed lines, which show clear descent from phases 5 to 6 and also phase 7, although a bit less clearly.

Analyzed stratospheric winds are poorly constrained close to the equator because wind measurements are scarce and the more abundant temperature sounding measurements do not constrain the wind where the Coriolis parameter becomes too small. (See section 2.2.) Figure 12b therefore repeats this analysis but includes only off-equatorial latitudes 10°–20°S, where the stratospheric wind is better constrained. The same pattern still appears although with slightly weaker amplitude.

We further contrast the winds in MERRA-2 (Figure 12b) with MERRA (Figure 12c). These look almost identical below 40 km where the reanalyses are well constrained by temperature sounding measurements. Above 40 km the reanalyses are poorly constrained by observations and will instead be more dependent on parameterized gravity wave drag. Differences appear at these higher altitudes that are likely because of the increase in MERRA-2 parameterized gravity wave stress equatorward of 15° (Molod et al., 2015). (See section 2.2.)

Given the big change in the parameterized gravity waves from MERRA to MERRA-2, we note that the strong similarities in Figures 12b and 12c below 40 km provide a confirmation that these anomalies are a real feature related to observational assimilation in the reanalyses and not simply created by the parameterized gravity wave drag, which is known to be highly uncertain. Thus, we expect similar wind anomalies below 40 km may be found in other reanalyses.

The waves observed by AIRS near 40 km are not contributing to drag below 40 km, but they will likely give drag above the observation level in the mesosphere or lower thermosphere (Eckermann et al., 1997). Wintertime intraseasonal winds near the mesopause have indeed been observed to exhibit stronger anomalies in the Eastern Hemisphere where the MJO is active than in the Western Hemisphere (Rao et al., 2009), so the intraseasonal gravity wave variations observed by AIRS may be driving such intraseasonal wind variations near the mesopause.

It is likely that the waves driving the stratospheric intraseasonal descending wind zones in Figure 12 are instead slower waves with shorter vertical wavelengths, like those observed in the Karoly et al. (1996) and Moss et al. (2016) studies. The lack of any obvious longitudinal variation of these winds suggests that the wave drag below 40 km may be caused by long horizontal wavelength gravity waves such as observed in Evan and Alexander (2008). That study revealed a large-amplitude, equatorially trapped wave with 2 day period and

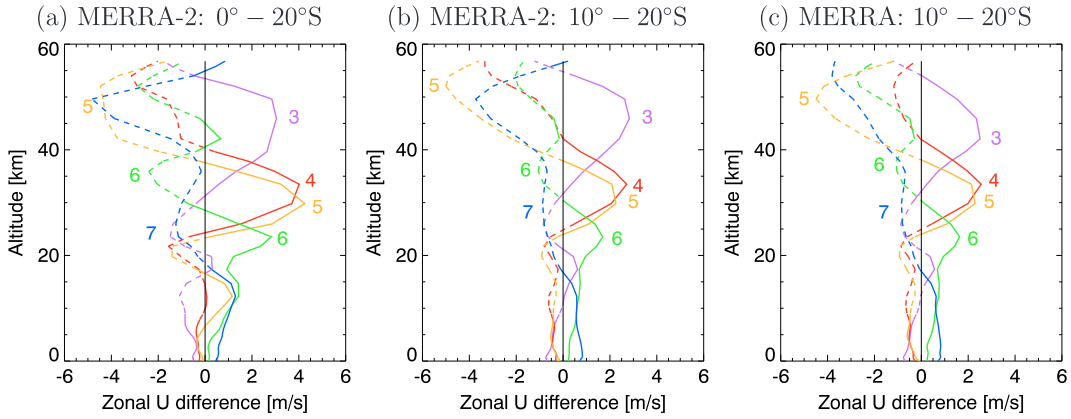

Figure 12. MJO-related zonal mean zonal winds at different MJO phases. (a) MERRA-2 zonal means of Figure 11. (b) MERRA-2 comparison including only latitudes 10°–20°S. (c) MERRA comparison including only latitudes 10°–20°S. Colors/numbers mark the phase of the MJO. Eastward winds are plotted with solid lines and westward winds with dashed lines. Figures 12b and 12c differ only above 40 km altitude in the lower mesosphere where there are little data constraining the reanalysis and where the changes in the parameterized gravity wave drag had their primary effect.

horizontal wavelength ~7,000 km (wave number ~ 6) with an apparent source region near the center of an MJO rain event (Evan et al., 2012).

Finally, we note that the eastward MJO wind anomalies descend to lower altitudes than the westward anomalies. This may indicate stronger amplitudes in MJO-related eastward waves in the lowermost stratosphere, which would be consistent with tropical western Pacific radiosondes (Gong et al., 2008), model studies (Alexander et al., 2017), and a case study of a large-amplitude inertia-gravity wave event tied to MJO convection (Evan et al., 2012). High-wave number Kelvin waves generated by MJO convection could also contribute. Further work would be needed to address the nature of the waves responsible for the stratospheric wind anomalies and any relationships to the phase of the QBO as suggested by the results in Moss et al. (2016).

6. Summary and Conclusions

MJO-related stratospheric gravity wave variance as observed by AIRS is anticorrelated with tropopause zonal wind U_{100}, and we investigate the origin of this anticorrelation. Idealized model simulations that use the same convective gravity wave sources but vary the winds show that AIRS gravity wave variance is primarily sensitive to changes in stratospheric zonal wind (Figure 8) due to their effects on gravity wave vertical wavelength (Figure 9). This is the observational filter effect. Tropopause wind has only a relatively small effect (~10%). Thus, neither tropopause wind filtering nor source effects are very important for waves observed by AIRS. Because MJO precipitation anomalies are associated with westward wind anomalies in the upper troposphere (Figures 11 and S1), the results suggest that this U_{100} relationship to precipitation is the origin of the anticorrelation between U_{100} and AIRS gravity wave variance.

Further evidence in reanalyzed winds shows that the gravity waves drive intraseasonal stratospheric zonal wind anomalies that descend in altitude with increasing MJO phases 3 through 7 (Figure 12). Descent is observed in both eastward and westward intraseasonal wind anomalies, but the eastward anomalies are stronger and descend to lower altitudes. This implies that both eastward and westward propagating gravity waves are generated by MJO-related precipitation. Because the eastward wind anomalies descend farther than the westward wind anomalies, we hypothesize that eastward propagating waves are generated with larger amplitudes to give larger drag forces than westward waves. Large-amplitude eastward propagating waves might be expected if there is a significant obstacle effect or "moving mountain" mechanism that generates MJO-related convective gravity waves. These waves would have slow phase speeds c_0 associated with the motions of individual rain cells within the MJO precipitation envelope, or $c_0 \sim 5$ m s^{-1} associated with the speed of the MJO envelope itself. Our results show that while slow waves with $c < 10$ m s^{-1} do not contribute much to AIRS observations of gravity wave variance in December–March, they may contribute to gravity wave variance observed with radio occultation or radiosonde methods (Evan et al., 2012; Karoly et al., 1996; Moss et al., 2016), and they are likely to be important to driving the MJO wind anomalies below 40 km seen in the MERRA and MERRA-2 reanalyses (Figure 12).

Acknowledgments
This work was supported by the National Science Foundation with grants 1318932 and 1519271 from the Physical and Dynamical Meteorology and Climate and Large-scale Dynamics Programs. The Gunn Point radar data were generated by Michael Whimpey and distributed by Peter May at the Australian Bureau of Meteorology. MERRA and MERRA-2 winds and temperatures, AIRS level 1B Infrared Radiances, and TRMM 3B42 Precipitation Rates were obtained freely from NASA Goddard Earth Science's Data Information Services Center (https://disc.sci.gsfc.nasa.gov), daily RMM MJO Index data from the Australian Bureau of Meteorology (http://www.bom.gov.au/climate/mjo/), and daily GPCP data from NASA's Mesoscale Atmospheric Processes science research portal (https://precip.gsfc.nasa.gov).

References

Alexander, M. J. (1998). Interpretations of observed climatological patterns in stratospheric gravity wave variance. *Journal of Geophysical Research*, *103*, 8627–8640.

Alexander, M. J., Ortland, D. A., Grimsdell, A. W., & Kim, J.-E. (2017). Sensitivity of gravity wave fluxes to interannual variations in tropical convection and zonal wind. *Journal of Atmospheric Sciences*, *74*, 2701–2716. https://doi.org/10.1175/JAS-D-17-0044.1

Alexander, M. J., Richter, J. H., & Sutherland, B. R. (2006). Generation and trapping of gravity waves from convection, with comparison to parameterization. *Journal of Atmospheric Sciences*, *63*(11), 2963–2977.

Baker, W. E., Atlas, R., Cardinali, C., Clement, A., Emmitt, G. D., Gentry, B. M., … Yoe, J. G. (2014). Lidar-measured wind profiles: The missing link in the global observing system. *Bulletin of the American Meteorological Society*, *95*(4), 543–564. https://doi.org/10.1175/BAMS-D-12-00164.1

Beres, J., Alexander, M. J., & Holton, J. R. (2004). A method of specifying the gravity wave spectrum above convection based on latent heating properties and background wind. *Journal of Atmospheric Sciences*, *61*, 324–337.

Bosilovich, M. G., Lucchesi, R., & Suarez, M. (2015). MERRA-2: File specification, GMAO Office Note No. 8 (version 1.3, 73 pp.). Retrieved from http://gmao.gsfc.nasa.gov/pubs/office_notes

Dunkerton, T. (1997). The role of gravity waves in the quasi-biennial oscillation. *Journal of Geophysical Research*, *102*, 26,053–26,076.

Eckermann, S. D., Rajopadhyaya, D. K., & Vincent, R. A. (1997). Intraseasonal wind variability in the equatorial mesosphere and lower thermosphere: Long-term observations from the central Pacific. *Journal of Atmospheric and Solar-Terrestrial Physics*, *59*, 603–627.

Evan, S., & Alexander, M. J. (2008). Intermediate-scale tropical inertia gravity waves observed during TWP-ICE campaign. *Journal of Geophysical Research*, *113*, D14104. https://doi.org/10.1029/2007JD009289

Evan, S., Alexander, M. J., & Dudhia, J. (2012). Model study of intermediate-scale tropical inertia-gravity waves and comparison to TWP-ICE campaign observations. *Journal of Atmospheric Sciences*, *69*, 591–610. https://doi.org/10.1175/JAS-D-11-051.1

Fritts, D. C., & Alexander, M. J. (2003). A review of gravity wave dynamics and effects on the middle atmosphere. *Reviews of Geophysics*, *41*(1), 1003. https://doi.org/10.1029/2001RG000106

Garcia, R., Dunkerton, T., Lieberman, R., & Vincent, R. (1997). Climatology of the semiannual oscillation of the tropical middle atmosphere. *Journal of Geophysical Research*, *102*, 26,019–26,032.

Gelaro, R., McCarty, W., Suárez, M. J., Todling, R., Molod, A., Takacs, L., … Zhao, B. (2017). The Modern-Era Retrospective Analysis for Research and Applications, version 2 (MERRA-2). *Journal of Climate*, *30*(14), 5419–5454. https://doi.org/10.1175/JCLI-D-16-0758.1

Gong, J., Geller, M. A., & Wang, L. (2008). Source spectra information derived from U.S. high-resolution radiosonde data. *Journal of Geophysical Research*, *113*, D10106. https://doi.org/10.1029/2007JD009252

Grimsdell, A. W., Alexander, M. J., May, P., & Hoffmann, L. (2010). Model study of waves generated by convection with direct validation via satellite. *Journal of Atmospheric Sciences*, *67*, 1617–1631.

Hoffmann, L., & Alexander, M. J. (2009). Retrieval of stratospheric temperatures from AIRS radiance measurements for gravity wave studies. *Journal of Geophysical Research*, *114*, D07105. https://doi.org/10.1029/2008JD011241

Hoffmann, L., & Alexander, M. J. (2010). Occurrence frequency of convective gravity waves during the North American thunderstorm season. *Journal of Geophysical Research*, *115*, D20111. https://doi.org/10.1029/2010JD014401

Hoffmann, L., Alexander, M. J., Clerbaux, C., Grimsdell, A. W., Meyer, C. I., Rößler, T., & Tournier, B. (2014). Intercomparison of stratospheric gravity wave observations with AIRS and IASI. *Atmospheric Measurement Techniques*, *7*(12), 4517–4537. https://doi.org/10.5194/amt-7-4517-2014

Holt, L. A., Alexander, M. J., Coy, L., Molod, A., Putman, W., & Pawson, S. (2016). Tropical waves and the quasi-biennial oscillation in a 7-km global climate simulation. *Journal of Atmospheric Sciences*, *73*, 3771–3783. https://doi.org/10.1175/JAS-D-15-0350.1

Huffman, G., Adler, R. F., Morrissey, M., Bolvin, D. T., Curtis, S., Joyce, R., … Susskind, J. (2001). Global precipitation at one-degree daily resolution from multi-satellite observations. *Journal of Hydrometeorology*, *2*, 36–50.

Huffman, G. J., Adler, R. F., Bolvin, D. T., Gu, G., Nelkin, E. J., Bowman, K. P., … Wolff, D. B. (2007). The TRMM multisatellite precipitation analysis (TNPA): Quasi-global, multiyear, combined-sensor precipitation estimates at fine scales. *Journal of Hydrometeorology*, *8*, 38–55.

Jensen, E., & Pfister, L. (2004). Transport and freeze drying in the tropical tropopause layer. *Journal of Geophysical Research*, *109*, D02207. https://doi.org/10.1029/2003JD004022

Jiang, X., Waliser, D. E., Xavier, P. K., Petch, J., Klingaman, N. P., Woolnough, S. J., … Zhu, H. (2015). Vertical structure and physical processes of the Madden-Julian Oscillation: Exploring key model physics in climate simulations. *Journal of Geophysical Research: Atmosphere*, *120*, 4718–4748. https://doi.org/10.1002/2014JD022375

Karoly, D., Roff, G., & Reeder, M. (1996). Gravity wave activity associated with tropical convection detected in TOGA COARE sounding data. *Geophysical Research Letters*, *23*(3), 261–264.

Keenan, T., Glasson, K., Cummings, T., Keeler, J., & Lutz, J. (1998). The BMRC/NCAR C-band polarimetric (C-POL) radar system. *Journal of Atmospheric and Oceanic Technology*, *15*, 871–886.

Kim, J.-E., & Alexander, M. J. (2015). Direct impacts of waves on tropical cold point tropopause temperature. *Geophysical Research Letters*, *42*, 1584–1592. https://doi.org/10.1002/2014GL062737

Madden, R., & Julian, P. (1994). Observations of the 40-50-day tropical oscillation—A review. *Monthly Weather Review*, *122*, 814–837.

May, P. T., Mather, J., Vaughan, G., Jakob, C., McFarquhar, G., Bower, K. N., & Mace, G. G. (2007). Keynote: The Tropical Warm Pool International Cloud Experiment (TWPICE), 33rd Conference on Radar Meteorology, Cairns, Australia, August 10, 2007, 12A.1. Retrieved from https://ams.confex.com/ams/33Radar/techprogram/paper_122333.htm

Molod, A., Takacs, L., Suarez, M., & Bacmeister, J. (2015). Development of the GEOS-5 atmospheric general circulation model: Evolution from MERRA to MERRA2. *Geoscientific Model Development*, *8*, 1339–1356. https://doi.org/10.5194/gmd-8-1339-2015

Moss, A. C., Wright, C. J., & Mitchell, N. J. (2016). Does the Madden-Julian Oscillation modulate stratospheric gravity waves? *Geophysical Research Letters*, *43*, 3973–3981. https://doi.org/10.1002/2016GL068498

Pfister, L., Chan, K. R., Bui, T. P., Bowen, S., Legg, M., Gary, B., … Starr, W. (1993). Gravity waves generated by a tropical cyclone during the STEP tropical field program: A case study. *Journal of Geophysical Research*, *98*, 8611–8638.

Podglajen, A., Hertzog, A., Plougonven, R., & Žagar, N. (2014). Assessment of the accuracy of (re)analyses in the equatorial lower stratosphere. *Journal of Geophysical Research: Atmospheres*, *119*, 11,166–11,188. https://doi.org/10.1002/2014JD021849

Rao, R. K., Gurubaran, S., Sathishkumar, S., Sridharan, S., Nakamura, T., Tsuda, T., … Mitchell, N. J. (2009). Longitudinal variability in intraseasonal oscillation in the tropical mesosphere and lower thermosphere region. *Journal of Geophysical Research*, *114*, D19110. https://doi.org/10.1029/2009D011811

Ray, E., Alexander, M., & Holton, J. (1998). An analysis of the structure and forcing of the equatorial semiannual oscillation in zonal wind. *Journal of Geophysical Research*, *103*, 1759–1774.

Rienecker, M. M., Suarez, M. J., Gelaro, R., Todling, R., Bacmeister, J., Liu, E., … Woollen, J. (2011). MERRA: NASA's Modern-Era Retrospective Analysis for Research and Applications. *Journal of Climate*, *24*, 3624–3648.

Scaife, A., Butchart, N., Warner, C., Stainforth, D., & Norton, W. (2000). Realistic quasi-biennial oscillations in a simulation of the global climate. *Geophysical Research Letters*, *27*(21), 3481–3484.

Scaife, A. A., Arribas, A., Blockley, E., Brookshaw, A., Clark, R. T., Dunstone, N., … Williams, A. (2014). Skillful long-range prediction of European and North American winters. *Geophysical Research Letters*, *41*, 2514–2519. https://doi.org/10.1002/2014GL059637

Stephan, C., & Alexander, M. J. (2015). Realistic simulations of atmospheric gravity waves over the continental U.S. using precipitation radar data. *Journal of Advances in Modeling Earth Systems*, *7*(2), 823–835. https://doi.org/10.1002/2014MS000396

Stephens, G. L. (2005). Cloud feedbacks in the climate system: A critical review. *Journal of Climate*, *18*(2), 237–273. https://doi.org/10.1175/JCLI-3243.1

Thompson, D. W., Baldwin, M. P., & Wallace, J. M. (2002). Stratospheric connection to Northern Hemisphere wintertime weather: Implications for prediction. *Journal of Climate* , *15*, 1421–1428. https://doi.org/10.1175/1520-0442(2002)015<1421:SCTNHW>2.0.CO;2

Tsuchiya, C., Sato, K., Alexander, M. J., & Hoffmann, L. (2016). MJO-related intraseasonal variation of gravity waves in the Southern Hemisphere tropical stratosphere revealed by high-resolution AIRS observations. *Journal of Geophysical Research: Atmospheres*, *121*, 7641–7651. https://doi.org/10.1002/2015JD024463

Waliser, D., Sperber, K., Hendon, H., Kim, D., Maloney, E., Wheeler, M., … Woolnough, S. (2009). MJO simulation diagnostics. *Journal of Climate*, *22*, 3006–3030. https://doi.org/10.1175/2008JCLI2731.1

Wheeler, M. C., & Hendon, H. H. (2004). An all-season real-time multivariate MJO index: Development of an index for monitoring and prediction. *Monthly Weather Review*, *132*(8), 1917–1932. https://doi.org/10.1175/1520-0493(2004)132<1917:AARMMI>2.0.CO;2

Wheeler, M. C., & Hendon, H. H. (2016). Real-time multivariate Madden-Julian-Oscillation (RMM) index, Retrieved from http://www.bom.gov.au/climate/mjo/.

Xie, P., Adler, R. F., Huffman, G., & Bolvin, D. (2011). Global precipitation climatology project—Pentad, version 2.2. NOAA National Climatic Data Center. Accessed January 2017.

Žagar, N., Isaksen, L., Tan, D., & Tribbia, J. (2013). Balance properties of the short-range forecast errors in the ECMWF 4D-Var ensemble. *Quarterly Journal of the Royal Meteorological Society*, *139*(674), 1229–1238. https://doi.org/10.1002/qj.2033

Zhang, C. (2005). Madden-Julian Oscillation. *Reviews of Geophysics*, *43*, RG2003. https://doi.org/10.1029/2004RG000158